Progress In Electromagnetics Research M, Vol. 118, 71–82, 2023

Improved Side-Lobe Suppression by Optimizing the Beam Synthetization in Uniform Circular Arrays for OAM Generation

Layth Abogneem, Ahmad Alamayreh, and Nidal Qasem*

Abstract—Enhancing the capacity of wireless communications systems is necessary to manage growing networks. Thus, this work presents an analytical model for describing the deterioration in orbital angular momentum (OAM). The proposed model is based on a uniform circular array, which can be applied in OAM generation to obtain the desired beam properties. First, the side-lobe problem in OAM applications is examined and resolved by optimizing the beam synthetization. Then, comparisons between the two window techniques are used to evaluate their impacts. Finally, the effects of selecting the optimal window technique and width on the solutions are investigated. Numerical results and the comparisons between derived formulas and those obtained via full-wave numerical simulations are shown.

1. INTRODUCTION

Recent developments in radio communications systems have drawn the attention of many academics and researchers in the area of orbital angular momentum (OAM) applications [1, 2]. The role of capacity in various applications is critical, namely mobile communications [3, 4], radar [5–7], and satellite communications [8–10]. Each OAM order (l) carries data, thus multiple OAM orders can be used to enhance the capacity of the system [11, 12]. Furthermore, there are numerous options for OAM order generation, such as optics [13], spoof surface plasmon [14], spiral phase plates [15], metasurface [16], and uniform circular array (UCA) generation [17–19]. However, there are several limitations and outstanding issues in OAM generation, including null divergence [20, 21] and side-lobe interference [22, 23].

The first example of side-lobe interference is when the side lobes of different order beams interfere at the same location (i.e., if the smaller order is in the null of the larger order and there is a high side-lobe level in the small order). This causes an effect and distortion in the higher order [24]. Another example is when multiple beams are located at different places and interact after a certain distance (i.e., if there are arbitrary OAM superpositions), which leads to ambiguity between the beams [25]. To address this gap in OAM research, several techniques have been presented [26–28].

In [26], phased array technology is used to direct vortex beams created by a UCA, and the main lobe of the vortex beams with different modes produced by the same UCA can illuminate the probed target, leading to a higher resolution. In [27], time-modulated concentric circular arrays (TMCCAs) are used to generate various OAM modes at discrete sideband harmonic frequencies and achieve beam steering at the first harmonic frequency. Furthermore, beam steering for OAM beams is accomplished without the need for expensive phase shifters in phased arrays by employing switches attached to array elements, and thus this method is relatively simple and inexpensive. In [28], a chamfer antenna array is constructed for generating the detected circular polarized OAM vortex beam with minimal side lobes using phased array technology, and the antenna array synthesis approach based on the Chebyshev amplitude distribution was used to suppress the side-lobe level. In [29], TMCCAs are used to create

Received 23 May 2023, Accepted 14 July 2023, Scheduled 27 July 2023
* Corresponding author: Nidal Qasem (Ne.qasem@ammanu.edu.jo).
The authors are with the Communications and Computer Engineering Department, Al-Ahliyya Amman University, Amman, Jordan.

OAM beams with lower side-lobe levels, and the optimized and non-optimized patterns are compared. The results reveal that the optimized pattern side-lobe levels are effectively suppressed. Notably, the synthesis OAM beams with low side-lobe levels is accomplished using simple RF switches. In [30], concentric-ring arrays are intended to attenuate the radiation pattern side lobes. Using the genetic algorithm, the results reveal that side lobes are successfully suppressed. One of the side-lobe level reduction techniques is tapering window functions which can provide very deep side-lobe levels [31]. Optimized tapering windows, such as Gaussian and cylinder windows [32, 33], are efficient at reducing side-lobe levels, especially for small-sized arrays. The Gaussian window, also called bell-shaped window, is considered one of adjustable windows, which offers a selectable trade-off between spectral resolution and band limitedness. Moreover, Gaussian window can be used to reduce the side lobe of a UCA [32]. On the other hand, cylinder window has ripples in frequency domain due to the sharp cutoff in the space domain [33]. The existence of ripples usually degrades the performance in the form of interference in many applications. In imaging or microscopy for instance, the minimum resolution between two nearby points depends on how far the spectrum of the points can be separated with as minimal interference as possible in the resulting spectrum.

The present work focuses on the effect of beamforming on OAM interference. We develop an analytical approach for managing the outer side lobes that appear when critical OAM orders get close to adjacent OAM orders. The key contributions are summarized as follows. First, we develop an analytical model for reducing and canceling the unwanted signals in OAM waves by multiplying them with a mask. Second, an extensive set of MATLAB simulations is performed to evaluate the impact of the window technique and width. Finally, the effects of selecting the optimal window technique and width on the solutions are investigated.

The remainder of this paper is structured as follows. Section 2 explains the proposed system model. Section 3 provides the numerical results and comparisons between derived formulas and those obtained via CST-MWS simulations. Then, the current work is compared with previous works. Finally, Section 4 concludes this study.

2. SYSTEM MODEL

This section presents a mathematical formula for the design and the generated wave to clarify the propagation properties of the radiation produced by the suggested approach. The primary beam was formed from an OAM order l Bessel beam. A Bessel function of the first kind and l^{th} order $J_l(\cdot)$ characterizes the beam magnitude in the transverse propagation plane. Therefore, in the cylindrical coordinates (ρ, φ, z), the beam has the shape $J_l(\beta\rho)e^{im\varphi}$, with β being the radial wavenumber, as defined by the separation relation, which connects the radial and longitudinal wave numbers with the properties of the medium. Owing to its unphysical properties, such as infinite total energy and an infinite range of propagation, the beam in this form is known as an ideal field. The Bessel-Gauss amplitude is a common depiction of such a model. In this case, the Bessel beam is modified by a Gaussian with a waist radius of W_o in $e^{\frac{-\rho^2}{W_o}}$, where $\rho = \sqrt{x^2 + y^2}$.

This work presents a UCA that can be used for generating an OAM vortex wave to obtain the desired beam properties. Then, to resolve the OAM limitations caused by side lobes, we apply the window technique to smooth and obtain clear waves without ripples. Next, the desired field is calculated from Eq. (10). After that, we perform back-propagation to obtain the near field. Then, from the near field, we extract the amplitude and phase that are then fed to the CST-MWS to validate and match the numerical results and CST-MWS. Table 1 displays the fundamental parameters chosen for the proposed UCA.

Table 1. Fundamental parameters for UCA.

Parameter	Value
Number of dipole antenna elements (N)	8
Frequency (f_r)	3 GHz
Radius (R)	3.7 cm

Using a UCA, the far field is the superposition of radiation from N-dipoles, with the radiation of the n^{th} dipole in the form [2]:

$$E_n = \frac{e^{(il\varphi_n)}e^{(ikD_n)}}{D_n} \tag{1}$$

where E_n is the far field in the z-plane of the n^{th} dipole, $\varphi_n = \frac{2\pi}{N}n$ the location angle of the n^{th} dipole in that plane, l the OAM order, $k = \frac{2\pi}{\lambda}$ the wavenumber, λ the wavelength, N the number of array elements, i the location angle of the n^{th} radiation element, and D_n the distance from the UCA center, which is expressed as follows:

$$D_n = \sqrt{(z-0)^2 + (x - R\cos(\varphi_n))^2 + (y - R\sin(\varphi_n))^2} \tag{2}$$

where R is the UCA radius. Here, we use the back-propagation technique to synthesize the beam with the chosen OAM mode. This technique is powerful for the synthesis of wave fields in linear medium [30] and nonlinear medium [34]. It requires the knowledge of the medium of propagation between the UCA, or any general source, and the points where the field should be synthesized. Once the desired far field is determined, an appropriate numerical technique is applied to compute the excitation signals that the UCA elements must be fed to emit the desired far field. This method is not the key aim of this paper, but it ensures that the synthesized field is optimal for a given specification. The far field can be determined using the Fresnel diffraction formula [35]:

$$E_z(x,y,z) = -\frac{i}{\lambda z}e^{ikz}e^{\frac{ik}{2z}(x^2+y^2)}\iint E_o\left(x',y'\right)e^{\frac{ik}{2z}\left(x'^2+y'^2\right)}e^{\frac{-i2\pi}{\lambda z}(x'x+y'y)}dx'dy' \tag{3}$$

where E_o is the desired field. Let $f_x = \frac{x}{\lambda z}$, and $f_y = \frac{y}{\lambda z}$, then:

$$E_z(x,y,z) = -\frac{i}{\lambda z}e^{ikz}e^{\frac{ik}{2z}(x^2+y^2)}\iint E_o\left(x',y'\right)e^{\frac{ik}{2z}\left(x'^2+y'^2\right)}e^{-i2\pi f_x x'}e^{-i2\pi f_y y'}dx'dy' \tag{4}$$

We can also use the Fourier-transform formula instead of the integral form used in Eq. (4) as:

$$\begin{aligned}&\iint E_z\left(x',y'\right)e^{\frac{ik}{2z}\left(x'^2+y'^2\right)}e^{-i2\pi f_x x'}e^{-i2\pi f_y y'}dx'dy' \\ =\ & F\left\{E_o(x',y')e^{\frac{ik}{2z}\left(x'^2+y'^2\right)}\right\}E_z(x,y,z) = -\frac{i}{\lambda z}e^{ikz}e^{\frac{ik}{2z}(x^2+y^2)}F\left\{E_o(x',y')e^{\frac{ik}{2z}\left(x'^2+y'^2\right)}\right\}\end{aligned} \tag{5}$$

To find the near field using the back-propagation Fresnel diffraction formula, we obtain $E_o(x',y')$ at the source by back-propagation diffraction and use the inverse Fourier-transform formula as follows:

$$E_o\left(x',y'\right) = (-i\lambda z)e^{ikz}e^{\frac{ik}{2z}\left(x'^2+y'^2\right)}F^{-1}\left\{E_z(x,y,z)e^{\frac{ik}{2z}(x^2+y^2)}\right\} \tag{6}$$

We can also use the integral form instead of the inverse Fourier-transform formula used in Eq. (6) as:

$$F^{-1}\left\{E_z(x,y,z)e^{\frac{ik}{2z}(x^2+y^2)}\right\} = \iint E_z(x,y,z)\,e^{\frac{ik}{2z}(x^2+y^2)}e^{i2\pi f_{x'}x'}e^{i2\pi f_{y'}y'}dxdy \tag{7}$$

where $f_{x'} = \frac{x'}{\lambda z}$ and $f_{y'} = \frac{y'}{\lambda z}$. The final expression can be rewritten as:

$$E_o\left(x',y'\right) = (-i\lambda z)\,e^{ikz}e^{\frac{ik}{2z}\left(x'^2+y'^2\right)}\iint E_z(x,y,z)\,e^{\frac{ik}{2z}(x^2+y^2)}e^{\frac{2\pi}{\lambda z}(x'^2+y'^2)}dxdy \tag{8}$$

Finally, we use the window technique to reduce and remove the side lobes in the OAM beam. This technique is useful for canceling the interference between adjacent orders, and we adopt the Gaussian window in this study. Thus, to obtain the desired far field, we define the Gaussian window as follows:

$$G_w(x,y) = e^{-\left(\frac{x^2+y^2}{Wo^2}\right)} \tag{9}$$

Then the synthesized far field after applying the Gaussian window for E_o:

$$E_{G_w} = E_o \times G_w \tag{10}$$

where G_w is the Gaussian distribution, and W_o is the Gaussian window width.

Figure 1 depicts the geometry of the aperture field distribution. The intended OAM beam is established at a specific distance and aligned parallel to the radiating aperture. The purpose of beam synthesis is to determine the aperture field distribution that produces the desired OAM beam. The strategy used in this study is based on a theoretical framework and procedures described in [36] and [37]. In the present work, we focus on controlling the beamwidth and suppressing the side-lobe level in the OAM wave.

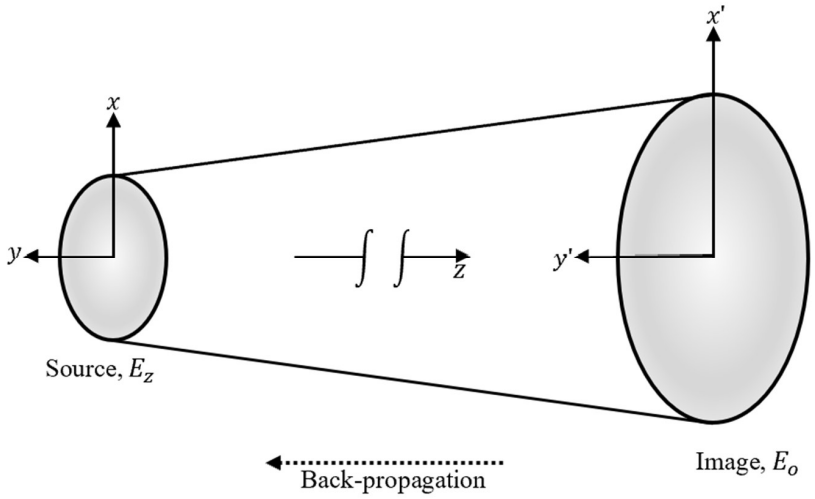

Figure 1. Proposed aperture field distribution geometry.

3. RESULTS AND DISCUSSION

In this section, numerical simulations are used to demonstrate the aims of this work. In the first step, we compare two windowing strategies to determine and adopt the optimal one for the remainder of the study. In the second step, we show the impact of the window width on interference removal by comparing multiple widths. The results obtained using MATLAB are validated by CST-MWS.

3.1. Comparison of Two Window Techniques

For the interference problem, more than one window technique is used, as shown in Figs. 2(a) and (b), but we observe several drawbacks in some windows; thus, we compare them and select the optimal one. Fig. 2(a) is obtained from Eq. (9), which illustrates a 2D Gaussian distribution. The equivalent frequency domain comparisons between the two windows with and without OAM are shown in Figs. 2(c) and (d), which are obtained from Eqs. (10) and (1), respectively. In these images, more ripples are observed in the cylindrical window drawn in the blue line because of the sharp cutoff, which will generate ripples in the frequency domain signal after windowing, but the Gaussian window drawn in the red line is smooth. Therefore, we employ the Gaussian window for the following experiments.

3.2. Eliminating Interference of the Side-lobe Level

Figure 3 shows multi-beams at $l = 1$ and 3, with and without the Gaussian window. It is easy to distinguish the different orders when we utilize a window, but it is harder when there is no window. Additionally, not only the usage window but selecting the window width is necessary, as shown in Fig. 4, which displays multi-beams at $l = 2$. Fig. 4(a) uses $W_o = 1.2$, and the thickness of the beam is wide, which leads to interference between beams because the window width is not appropriate. Fig. 4(b) uses $W_o = 0.8$, and the thickness of the beam is thin, but no interference is observed.

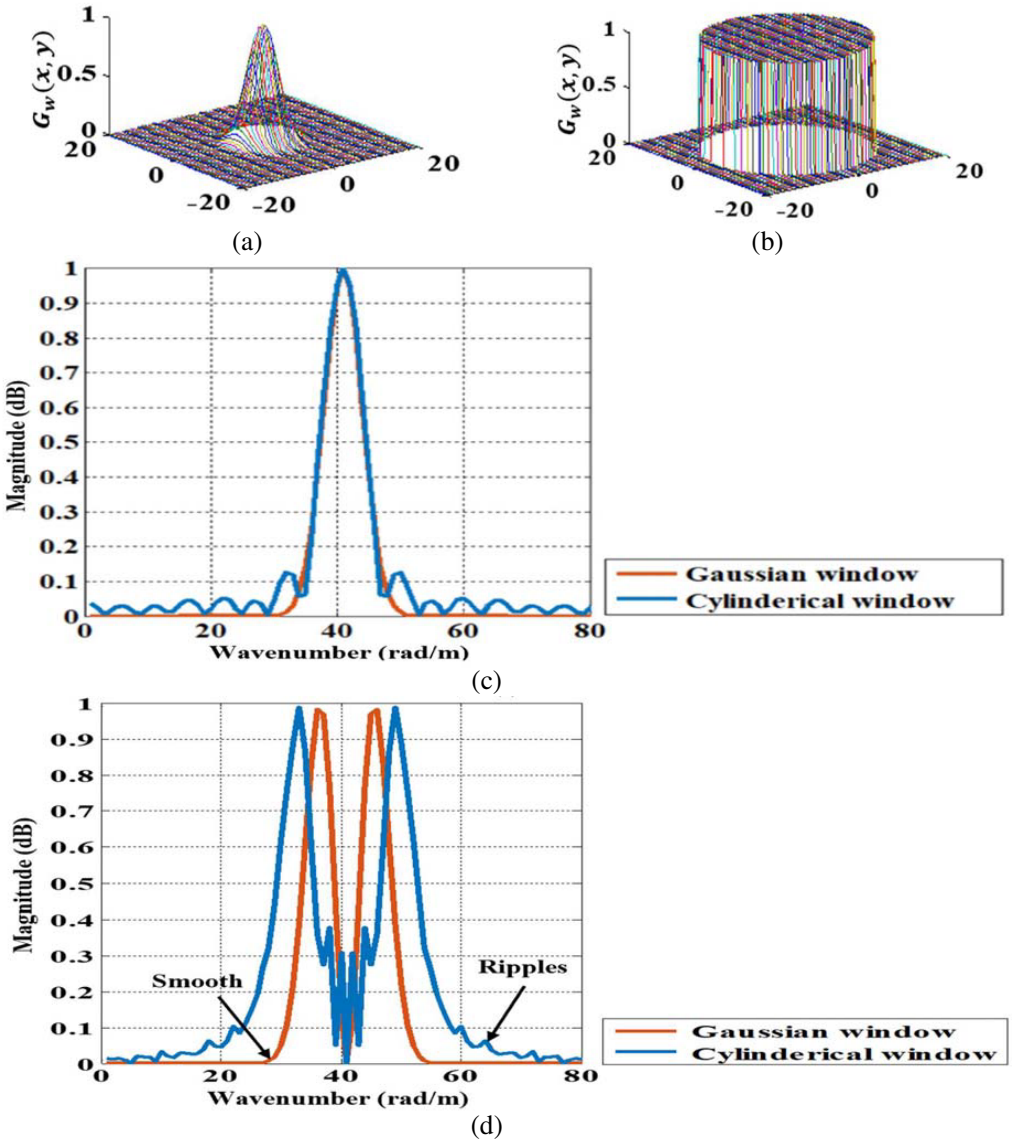

Figure 2. (a) 2D Gaussian distribution, (b) 2D cylindrical distribution, (c) comparison between two different windowing techniques in the frequency domain without OAM, and (d) comparison between two different windowing techniques in the frequency domain with OAM.

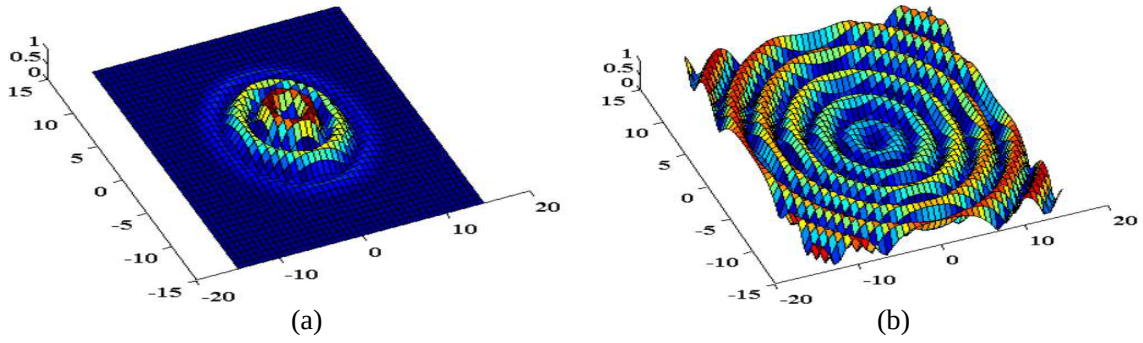

Figure 3. Multi-beams at $l = 1$ and 3 (a) with the window, and (b) without the window.

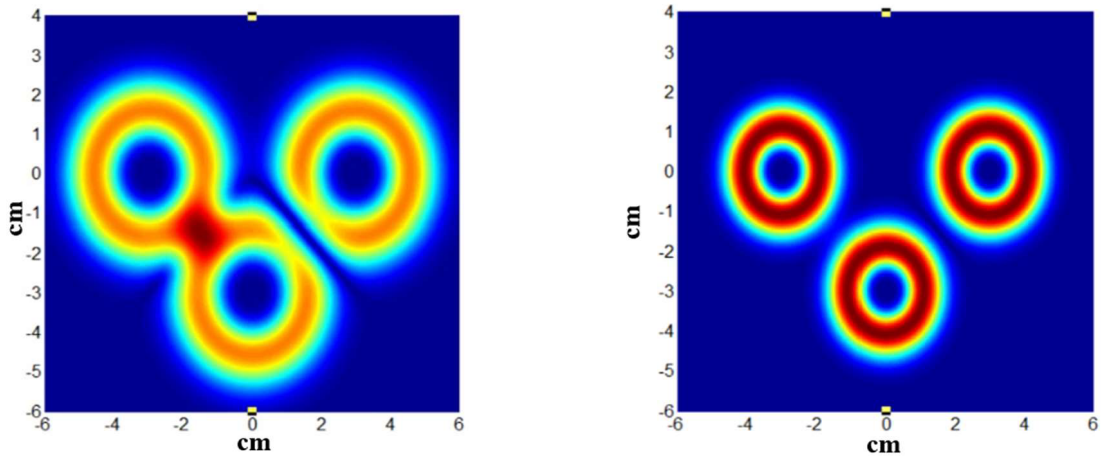

(a) (b)

Figure 4. Multi-beams at $l = 2$ for (a) $W_o = 1.2$ and (b) $W_o = 0.8$.

3.3. Comparison of Three Gaussian Widths and Selecting the Optimal One

In this subsection, the far-field numerical results obtained using MATLAB are investigated for the UCA with $N = 8$, $l = 4$ and with different Gaussian window widths normalized to lambda, as shown in Fig. 5.

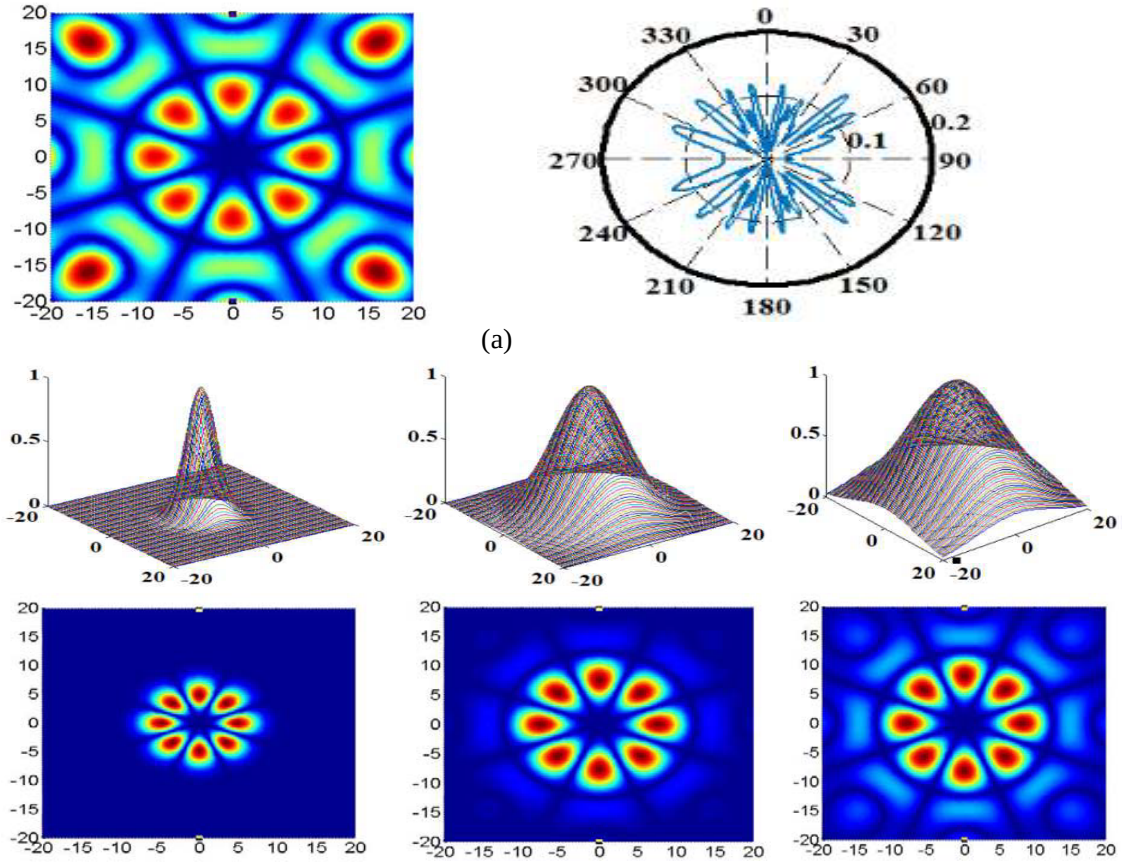

(a)

(b) (c) (d)

Figure 5. Far-field numerical results from MATLAB for the UCA with $N = 8, l = 4$, and for Gaussian windows with different W_o normalized to lambda; (a) without window, (b) $W_o = 4$, (c) $W_o = 10$, and (d) $W_o = 15$.

Fig. 5(a) shows that distortion and interference occur around the ring beams when no window is used. The comparison of $W_o = 4$, 10, and 15 is shown in Figs. 5(b), (c), and (d), respectively. When W_o is equal to 4, the window is small and does not cover the antenna element positions, causing distortion and some radiation cancelation, which is not a favorable condition. It is also problematic when W_o equals 15, allowing interference to flow through. Finally, the optimal solution for canceling interference is achieved using W_o equal to 10. From these three situations, we deduce that the lack of a window with OAM beams results in ripples. However, the window may cause another issue, and we must choose a suitable window width that covers the antenna element positions.

To demonstrate the numerical results obtained from MATLAB, numerical verification is performed using CST-MWS, as shown in Fig. 6. The purple line should represent the worst-case scenario when utilizing a beam without a window, which results in interference and distortion due to a critical order based on the number of elements. However, when an inappropriate Gaussian width is used, as shown by the blue line, the outcomes may be worse than the worst-case situation. We employ a window with a very small width for the orange line, which does not cover the UCA elements, resulting in distortion. However, when a suitable Gaussian width is chosen, as illustrated by the red line, interference is low.

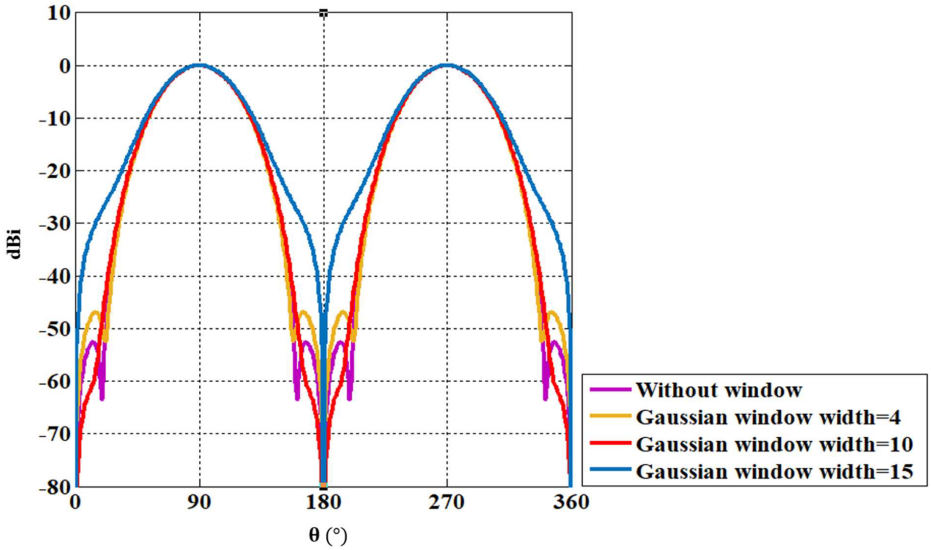

Figure 6. Far-field CST-MWS results for the UCA with $N = 8$, $l = 4$, and for Gaussian windows $W_o = 4$ (orange), $W_o = 10$ (red), $W_o = 15$ (blue), and without W_o (purple).

3.4. Implementing the Result with a Practical Frequency

To simulate and verify the results using a practical frequency, the far-field numerical results are obtained using MATLAB for a UCA with the following parameters: $N = 8$, $l = 2$, $W_o = 10$, $f_r = 3\,\text{GHz}$, and $R = 3.7\,\text{cm}$. As shown in Fig. 7(a), the yellow color represents the interference surrounding the ring of the beam in red, which is due to the absence of a window. Fig. 7(b) shows that the yellow color vanishes, and only the red color emerges because of the window. Finally, Fig. 7(c) represents the phase, so when the window is used and the interference is enhanced, the phase is still found, and no change is observed. These numerical results have been simulated using CST-MWS in Fig. 8, where Figs. 8(a) and (b) display the phase and intensity without a window (left) and with a window (right), respectively.

As can be observed in Figs. 7 and 8, there is a discrepancy between the results produced using MATLAB (see Fig. 7) and CST-MWS (see Fig. 8), with the difference primarily located in the outside region far from the origin. This is due to how both simulators handle boundary conditions. In MATLAB, the limits are defined by the size of the observation window. The window edges are not handled improperly. The open (add space) boundary condition has been set in CST-MWS, which automatically adds some extra space between the structure and the applied open boundary. It acts similarly to free

space but adds additional space for far-field calculations. Anyhow, we were concerned about the area around the center since we were interested in the UCA's excitement.

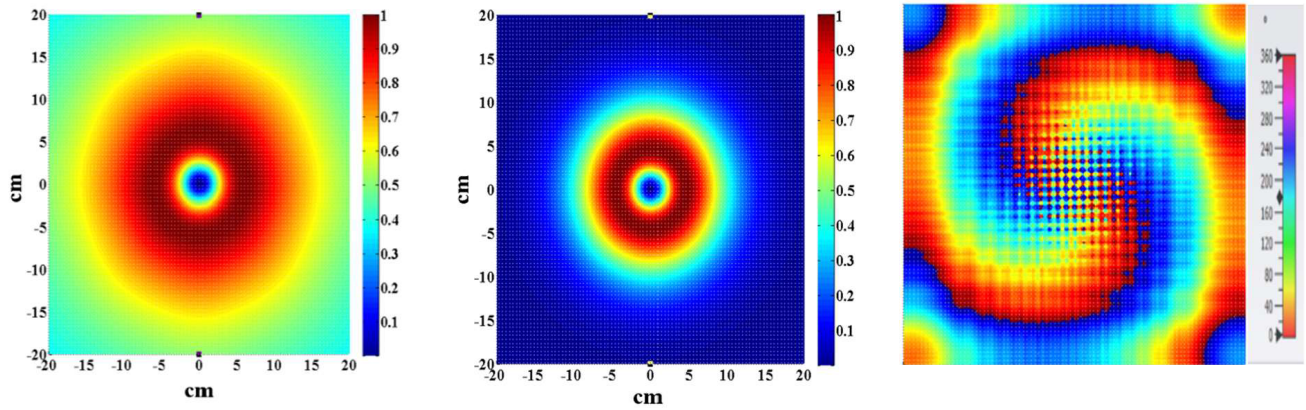

Figure 7. Far-field MATLAB numerical result for the UCA with $N = 8, l = 2$, for $W_o = 10$ ($f_r = 3\,\text{GHz}$, $R = 3.7\,\text{cm}$) (a) without a window, (b) with a window, and showing the (c) phase.

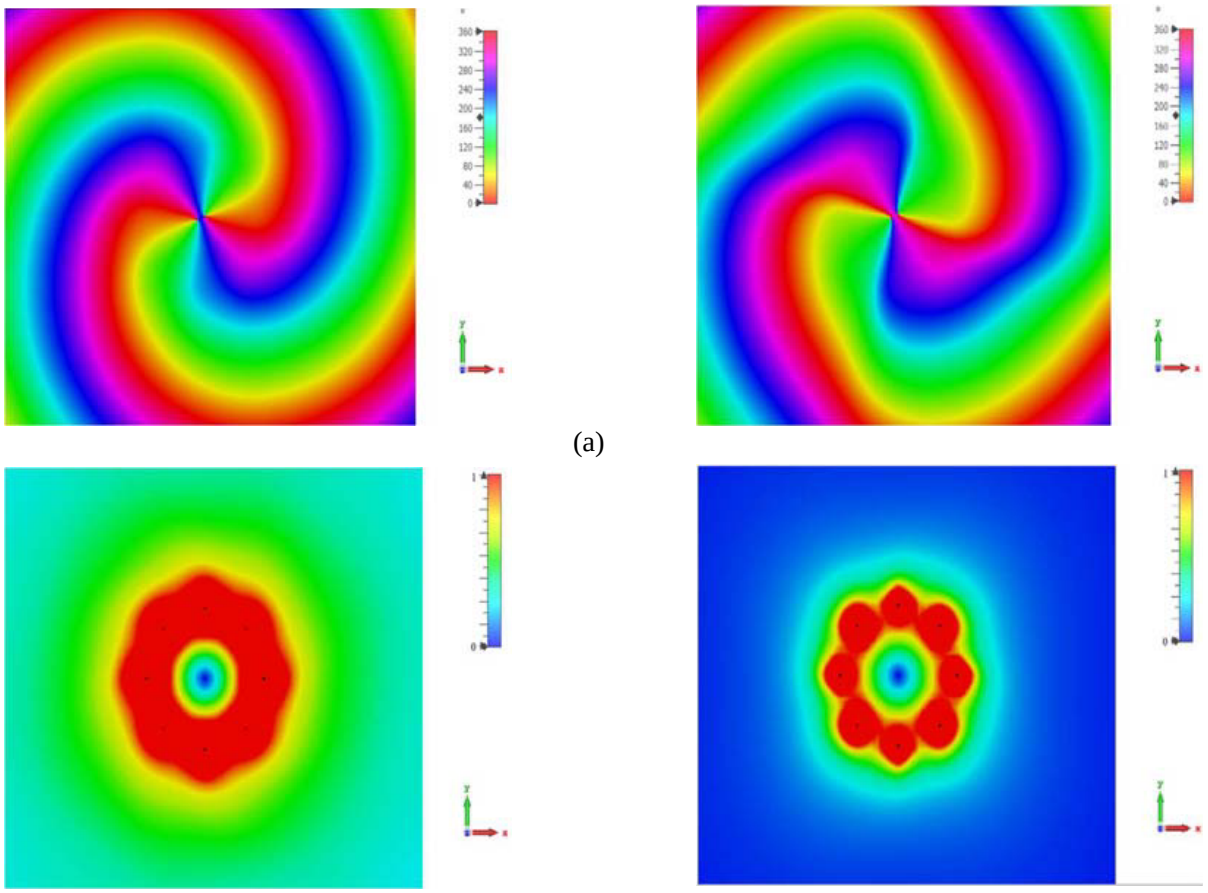

Figure 8. Far-field CST-MWS results for the UCA with $N = 8, l = 2$, for $W_o = 10$ ($f_r = 3\,\text{GHz}$, $R = 3.7\,\text{cm}$) without a window (left) and with a window (right); (a) phase and (b) intensity.

MATLAB considers the source, a dipole antenna, as a point source whose radiation is implemented using the dipole radiation formula from Eq. (1), and the CST-MWS provides accurate 3D electromagnetic solutions for the numerical solution of microwave design. It considers the physical properties of materials used in design for optimal solutions, a feature unavailable in MATLAB, which focuses primarily on the numerical translation of equations. This explains why the CST-MWS results in this scenario are not as impressive as the MATLAB results.

Figures 9(a) and (b) display the phase and intensity results, respectively, for the far-field CST-MWS results for the UCA without a Gaussian window using the following parameters: $N = 8$, $l = 4$, $f_r = 3\,\text{GHz}$, and $R = 3.7\,\text{cm}$. In Fig. 10, where three cases of beams are presented, we see that the resolution of Fig. 10(b) is higher than that of Figs. 10(a) and (c) because Fig. 10(a) has the same N as Fig. 10(b) but a smaller R, and Fig. 10(c) has the same R but a smaller N. We deduce that increasing N with a fixed R or decreasing R with a fixed N is necessary to improve resolution.

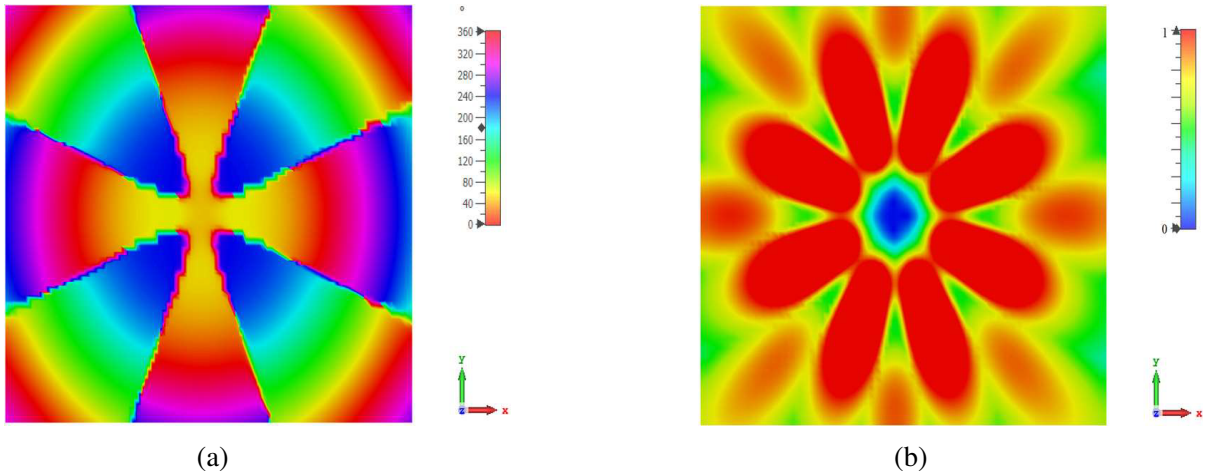

(a) (b)

Figure 9. Far-field CST-MWS results for the UCA with $N = 8$, $l = 4$, ($f_r = 3\,\text{GHz}$, $R = 3.7\,\text{cm}$) without a window; (a) phase and (b) intensity.

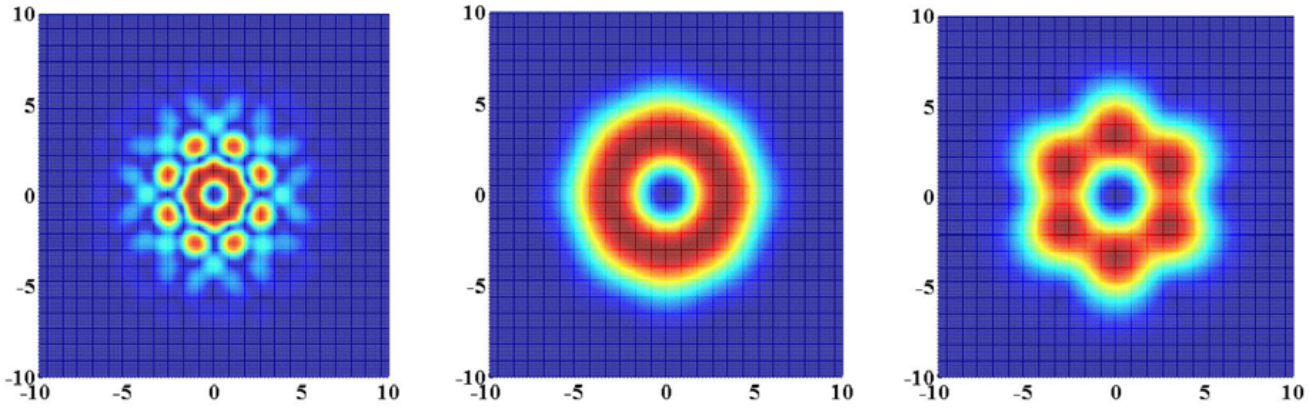

(a) (b) (c)

Figure 10. Far-field numerical results from MATLAB for the UCA with $l = 2$ for $W_o = 10$ normalized to lambda; (a) $N = 8$, $R = 20 * \lambda$, (b) $N = 8$, $R = 5 * \lambda$; and (c) $N = 6$, $R = 5 * \lambda$.

Next, Table 2 provides a comparison of prior works concerning the OAM side-lobe problem reported in [27–30] with respect to array form, OAM order, and side-lobe level considered. The study in [27] demonstrated the generation of OAM modes at harmonic frequencies and the beam steering for OAM beams at the first harmonic using time-modulated concentric circular arrays (TMCCAs). This study

Table 2. Comparison between the proposed technique and previous works.

References	Array form	OAM order	Side-lobe level
[27]	TMCCAs	1	Approx. −5 dB
[28]	Chamfer antenna array	1	Approx. −13 dB
[29]	TMCCAs	1, 2	Approx. −20 dB
[30]	UCA	1, 2, 3	Approx. −25 dB
This work	UCA	1, 2, 3, 4	Approx. −60 dB

lacked an optimization technique, resulting in the worst side-lobe level. In [28], a chamfer antenna array was designed for generating the deflected circular polarized OAM vortex beam with low side-lobe level. In order to suppress the side-lobe level, the antenna array synthesis method based on the Chebyshev amplitude distribution was adopted. The study in [29] demonstrated an OAM beam synthesis method based on TMCCAs. For equal-amplitude excitation TMCCAs, genetic algorithm (GA) was used to optimize the normalized switch-on duration of array elements. Results show that the side-lobe level of the optimized patterns is effectively suppressed. In [30], radiation pattern synthesis methods for the generation of vortex beams based on UCA were proposed. The optimized patterns using GA can significantly suppress side-lobe level. In summary, the proposed technique detailed in this work outperforms other techniques, which rely on selecting the correct width of Gaussian window based on the physical UCA radius.

4. CONCLUSIONS

In this work, OAM and beamforming technologies were combined to overcome the interference of the OAM channel capacity in modern wireless communications. Justifications for using a window were offered after we showed that separate beams can be stopped from interfering by using the appropriate window, and without the window, radiation interferes with each other. The Gaussian window was applied to all scenarios after showing that it was more effective than the circular window. We also demonstrated that using the proper window width is critical. Finally, we applied the proposed model in practice using CST-MWS and a practical frequency, $f_r = 3\,\text{GHz}$.

REFERENCES

1. Alamayreh, A. and N. Qasem, "Vortex beam generation in microwave band," *Progress In Electromagnetics Research C*, Vol. 107, 49–63, 2020.
2. Qasem, N. and A. Alamayreh, "Improved beam steering method using OAM wave," *Computer Systems Science and Engineering*, Vol. 4, No. 1, 417–431, 2023.
3. Chen, R., H. Du, and J. Li, "Indoor communications with OAM array," *2020 IEEE International Conference on Communications Workshops (ICC Workshops)*, 1–5, Dublin, Ireland, 2020.
4. Suganuma, H., S. Saito, K. Ogawa, and F. Maehara, "Effectiveness evaluation of dual-polarized OAM multiplexing employing SC-FDE in urban street canyon environments," *IEEE Access*, Vol. 10, 31934–31941, 2022.
5. Liu, H., K. Liu, Y. Cheng, and H. Wang, "Microwave vortex imaging based on dual coupled OAM beams," *IEEE Sensors Journal*, Vol. 20, 806–815, 2019.
6. Zeng, Y., Y. Wang, Z. Chen, J. Zhang, and J. Zhang, "Two-dimensional OAM radar imaging using uniform circular antenna array," *2020 14th European Conference on Antennas and Propagation (EuCAP)*, 1–4, Copenhagen, Denmark, 2020.
7. Liu, K., Y. Cheng, X. Li, Y. Qin, H. Wang, and Y. Jiang, "Generation of orbital angular momentum beams for electromagnetic vortex imaging," *IEEE Antennas and Wireless Propagation Letters*, Vol. 15, No. 16509284, 1873–1876, 2016.

8. Wang, Z., R. Malaney, and J. Green, "Satellite-based entanglement distribution using orbital angular momentum of light," *2020 IEEE International Conference on Communications Workshops (ICC Workshops*, 1–6, Dubli, Ireland, 2020.
9. Wang, Z., R. Malaney, and J. Green, "Detecting orbital angular momentum of light in satellite-to-ground quantum communications," *2019 IEEE Global Communications Conference (GLOBECOM)*, 1–6, Waikoloa, HI, USA, 2019.
10. Wang, Z., R. Malaney, and B. Burnett, "Satellite-to-earth quantum key distribution via orbital angular momentum," *Physical Review Applied*, Vol. 14, No. 6, 1–15, 2020.
11. Lyu, R., W. Cheng, W. Zhang, and F. Qin, "OAM-NFC: A short-range high capacity transmission scheme," *ICC 2020 — 2020 IEEE International Conference on Communications (ICC)*, 1–6, Dublin, Ireland, 2020.
12. Qasem, N., A. Alamayreh, and J. Rahhal, "Beam steering using OAM waves generated by a concentric circular loop antenna array," *Wireless Networks*, Vol. 27, 2431–2440, 2021.
13. Lian, Y., Y. Yu, S. Han, N. Luan, Y. Wang, and Z. Lu, "OAM beams generation technology in optical fiber: A review," *IEEE Sensors Journal*, Vol. 22, No. 5, 3828–3843, 2022.
14. Liao, Z., Y. Che, L. Liu, B. C. Pan, B. G. Cai, J. N. Zhou, G. O. Luo, and Y. Liu, "Reconfigurable vector vortex beams using spoof surface plasmon ring resonators," *IEEE Transactions on Antennas and Propagation*, Vol. 70, No. 8, 6795–6803, 2022.
15. Wei, H., A. K. Amrithanath, and S. Krishnaswamy, "3D printing of micro-optic spiral phase plates for the generation of optical vortex beams," *IEEE Photonics Technology Letters*, Vol. 31, No. 8, 599–602, 2019.
16. Guo, K., Q. Zheng, Z. Yin, and Z. Guo, "Generation of mode-reconfigurable and frequency-adjustable OAM beams using dynamic reflective metasurface," *IEEE Access*, Vol. 8, 75523–75529, 2020.
17. Yuan, T., Y. Cheng, H. Wang, and Y. Qin, "Beam steering for electromagnetic vortex imaging using uniform circular arrays," *IEEE Antennas and Wireless Propagation Letters*, Vol. 16, 704–707, 2017.
18. Chen, R., W. X. Long, X. Wang, and J. Li, "Multi-mode OAM radio waves: Generation, angle of arrival estimation and reception with UCAs," *IEEE Transactions on Wireless Communications*, Vol. 19, No. 10, 6932–6947, 2020.
19. Mohammadi, S. M., L. K. S. Daldorff, J. E. S. Bergman, R. L. Karlsso, B. Thide, K. Forozesh, and T. D. Carozzi, "Orbital angular momentum in radio — A system study," *IEEE Transactions on Antennas and Propagation*, Vol. 58, No. 2, 565–572, 2010.
20. Alamayreh, A., N. Qasem, and J. S. Rahhal, "General configuration MIMO system with arbitrary OAM," *Electromagnetics*, Vol. 40, No. 5, 343–353, 2020.
21. Qin, F., L. Li, Y. Liu, W. Cheng, and H. Zhang, "A four-mode OAM antenna array with equal divergence angle," *IEEE Antennas and Wireless Propagation Letters*, Vol. 18, No. 9, 1941–1945, 2019.
22. Alamayreh, A., N. Qasem, and J. S. Rahhal, "Pre-coding OAM based MIMO system for multi-user communications," *IEEE Access*, Vol. 10, 125411–125420, 2022.
23. Saito, S., Y. Ito, H. Suganum, K. Ogawa, and F. Maehara, "Efficient inter-mode interference cancellation method for OAM multiplexing in the presence of beam axis misalignment," *2021 IEEE International Conference on Communications Workshops (ICC Workshops)*, 1–6, Montreal, QC, Canada, 2021.
24. Cisternas, J. E., J. I. Espinoza, and J. A. Anguita, "Machine learning identification of multiple-state OAM superpositions detected with spatial mode sensors," *Laser Communication and Propagation through the Atmosphere and Oceans X*, Vol. 11834, 129–135, 2021.
25. Silva, B. P. D., B. A. D. Marques, R. B. Rodrigues, P. H. S. Ribeiro, and A. Z. Khoury, "Machine-learning recognition of light orbital-angular-momentum superpositions," *Physical Review A*, Vol. 103, No. 6, 063704, 2021.
26. Yuan, T., Y. Cheng, H. Wang, and Y. Qin, "Beam steering for electromagnetic vortex imaging using uniform circular arrays," *IEEE Antennas and Wireless Propagation Letters*, Vol. 16, 704–707, 2017.

27. Song, Q., Y. Wang, K. Liu, J. Zhang, and Y. Wang, "Beam steering for OAM beams using time-modulated circular arrays," *Electronics Letters*, Vol. 54, No. 17, 1017–1018, 2018.
28. Liang, J., Z. Jing, Q. Feng, Y. Zheng, and L. Li, "Synthesis and measurement of a circular-polarized deflection OAM vortex beam with sidelobe suppression array," *IEEE Access*, Vol. 8, 89143–89151, 2020.
29. Wang, Y., J. Liu, T. Hu, W. Jie, D. Yang, and A. Tennant, "Convergence of OAM beams using time-modulated concentric circular arrays," *2020 14th European Conference on Antennas and Propagation (EuCAP)*, 1–3, IEEE, Copenhagen, Denmark, 2020.
30. Liu, K., Y. Cheng, H. Wang, X. Li, and Y. Qin, "Radiation pattern synthesis for the generation of vortex electromagnetic wave," *IET Microwaves, Antennas & Propagation*, Vol. 11, No. 5, 685–694, 2017.
31. Albagory, Y. and F. Alraddady, "An efficient approach for sidelobe level reduction based on recursive sequential damping," *Symmetry*, Vol. 13, No. 3, 480, 2021.
32. Rahman, M., M. S. Islam, and M. F. Reza, "A higher immune tapered beamforming using Gaussian Window in the presence of amplitude errors," *2018 4th International Conference on Electrical Engineering and Information & Communication Technology (iCEEiCT)*, 577–580, IEEE, Dhaka, Bangladesh, 2018.
33. Prabhu, K. M. M., *Window Functions and Their Applications in Signal Processing*, Taylor & Francis, 2014.
34. Abo-Seida, O. M., N. T. M. El-Dabe, A. R. Ali, and G. A. Shalaby, "Cherenkov FEL reaction with plasma-filled cylindrical waveguide in fractional D-dimensional space," *IEEE Transactions on Plasma Science*, Vol. 49, No. 7, 2070–2079, 2021.
35. Goodman, J. W., *Introduction to Fourier Optics*, Roberts and Company Publishers, 2005.
36. Ettorre, M., M. Casaletti, G. Valerio, R. Sauleau, L. L. Coq, S. C. Pavone, and M. Albani, "On the near-field shaping and focusing capability of a radial line slot array," *IEEE Transactions on Antennas and Propagation*, Vol. 62, No. 4, 1991–1999, 2014.
37. Azevedo, J. A. R., "Synthesis of planar arrays with elements in concentric rings," *IEEE Transactions on Antennas and Propagation*, Vol. 59, No. 3, 839–845, 2011.